Soft Matter

Accepted Manuscript

ROYAL SOCIETY OF CHEMISTRY

www.rsc.org/softmatter

ARTICLE TYPE www. rsc.org/xxxxxx | XXXXXXXX

Rheology and Dynamics of Colloidal Superballs†

John R. Royer, ¶[a,b] **George L. Burton,**[a,c] **Daniel L. Blair,**[c] **and Steven D. Hudson***[a]

Received Xth XXXXXXXXXX 20XX, Accepted Xth XXXXXXXXX 20XX
First published on the web Xth XXXXXXXXXX 200X
DOI: 10.1039/b000000x
May 22, 2015

Recent advances in colloidal synthesis make it possible to generate a wide array of precisely controlled, non-spherical particles. This provides a unique opportunity to probe the role that particle shape plays in the dynamics of colloidal suspensions, particularly at higher volume fractions, where particle interactions are important. We examine the role of particle shape by characterizing both the bulk rheology and micro-scale diffusion in a suspension of pseudo-cubic silica superballs. Working with these well-characterized shaped colloids, we can disentangle shape effects in the hydrodynamics of isolated particles from shape-mediated particle interactions. We find that the hydrodynamic properties of isolated superballs are marginally different from comparably sized hard spheres. However, shape-mediated interactions modify the suspension microstructure, leading to significant differences in the self-diffusion of the superballs. While this excluded volume interaction can be captured with a rescaling of the superball volume fraction, we observe qualitative differences in the shear thickening behavior of moderately concentrated superball suspensions that defy simple rescaling on to hard sphere results. This study helps to define the unknowns associated with the effects of shape on the rheology and dynamics of colloidal solutions.

1 Introduction

There is a growing interest in anisotropic colloids,[1–3] while new synthesis techniques now make it possible to create a variety of different types of particles with uniform, well-controlled, non-spherical shapes. Simulations have shown that particle shape can have a dramatic effect on both the packing structure and equilibrium phase behavior of a material.[4–6] When used in combination with other interactions and functionalization schemes, particle shape can play a key role in the design of materials for self-assembly[7].

Despite this recent interest in anisotropic colloids, we are only beginning to understand how particle shape influences the rheology and micro-scale dynamics in a suspension. While previous studies have made progress understanding how particle shape influences the single-particle hydrodynamics,[8–13] this can only capture the first-order viscosity corrections in the dilute limit. Experiments exploring concentrated suspensions of colloidal[14] and non-Brownian[15] rods found significant shape effects, particularly in the shear thickening behavior, but there is no general theory to relate the microstructure and rheology in suspensions of anisotropic particles. This highlights a growing need for detailed experiments that can simultaneously probe both the bulk properties and micro-scale structure and dynamics in suspensions of well-controlled and well-characterized non-spherical particles.

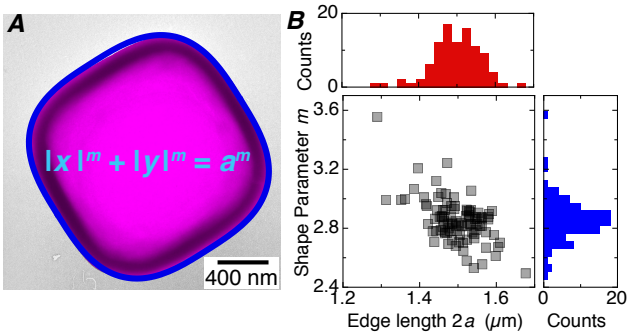

Fig. 1 Colloidal Superballs (A) Sample TEM image showing a hollow silica superball. The blue line shows a fit of the edge contour to $|x|^m + |y|^m = a^m$ to extract the shape parameter m and edge length $2a$. (B) Scatter plot of the shape parameter and edge length extracted from 96 TEM images from a single batch of cubes. Bar plots above and to the right show histograms of the same data.

† Electronic Supplementary Information (ESI) available: [details of any supplementary information available should be included here]. See DOI: 10.1039/b000000x/

[a] *Materials Science and Engineering Division, National Institute of Standards and Technology, Gaithersburg, MD 20899, USA*
[b] *Institute for Bioscience and Biotechnology Research (IBBR), University of Maryland, Rockville, MD 20850, USA*
[c] *Department of Physics and Institute for Soft Matter Synthesis and Metrology, Georgetown University, Washington, DC 20057, USA*
¶ Email:john.royer@nist.gov
* Email:steven.hudson@nist.gov

Here we work with suspensions of pseudo-cubic hollow-shell silica superballs,[16] colloidal particles with a shape well described by an equation of the form

$$|x|^m + |y|^m + |z|^m \leq a^m \quad (1)$$

where a characterizes the particle size and the exponent m is known as the shape parameter. For $m = 2$ this equation reduces to a sphere with radius a, while for $m > 2$ this equation describes cube-like shapes with rounded corners that approach sharp cubes as $m \to \infty$. Previous studies using similar particles focused on the self-assembly and crystal formation in quasi two-dimensional systems, using either depletion[16] or capillary forces[17] to induce attractive interactions between the superballs. Here we instead focus on three-dimensional suspensions without induced attraction to isolate the role of particle geometry. These particles are well-suited for exploring the role of particle shape because they are mono-disperse, readily dyed and index matched for confocal imaging, and can be synthesized in bulk quantities. This allows us to do both bulk rheology and, using confocal imaging, precisely locate and track particles to characterize the suspension microstructure and particle diffusion. Varying the volume fraction to explore both dilute and moderate concentrations, we find that these superballs behave similar to spheres at the single particle level but shape effects manifest themselves in the particle interactions.

2 Methods and Materials

Superball Synthesis

We synthesized hollow silica superballs following the approach initially described by Rossi *et al.*,[16], first synthesizing pseudo-cubic hematite ($\alpha-Fe_2O_3$) particles to serve as templates, then coating the hematite particles with a thin layer of silica using a modified Stöber process.[18] This silica shell is roughly 60 nm thick and porous, allowing fluid to slowly diffuse through the shell. We take advantage of this to etch away the hematite cores by placing the coated superballs in a strong acid. After 24 h to 48 h the cores are completely dissolved, leaving only the silica shells. Details of the synthesis procedure are provided in the SI.

In Fig. 1 we characterize the the size and shape of the hollow silica superballs used in this work. From TEM images of individual superballs (Fig. 1*A*) we use image processing routines to extract the contour of the of the outer edge. We then fit this contour to a 2D superball $|x|^m + |y|^m = a^m$ to extract the shape parameter m and edge length $L = 2a$. Repeating this procedure with multiple TEM images (Fig. 1*B*), we find that $\langle L \rangle = 1.50\ \mu\text{m} \pm 0.06\ \mu\text{m}$ and that $\langle m \rangle = 2.85 \pm 0.15$. From the variance of the measured edge length distribution $\langle \Delta L^2 \rangle$ we compute the polydispersity $s = \sqrt{\langle \Delta L^2 \rangle}/\langle L \rangle^2 = 0.04$, a rather low value compared to other colloidal systems.[19] Fluorescent and undyed superballs were made from a single batch of hematite templates and the resulting silica particles were indistinguishable in both size and shape.

Index matched suspensions of silica superballs were prepared using a glycerol/water mixture (92 % glycerol mass fraction, refractive index $n = 1.461$), with a small amount of added salt (NaCl) to screen electrostatic interactions (the Debye screening length is $\kappa^{-1} = 7$ nm). A detailed description of the index matching procedure for these hollow, porous shells is provided in the SI. Diffusion of the high viscosity index-matching fluid ($\mu = 0.29$ Pa·s at 21.0 °C) through the silica shells is exceptionally slow, so that the superballs can be considered as impermeable solid particles over the timescales for the diffusion and rheology measurements. This low permeability could also be exploited to image undyed superballs by fluorescently dyeing the outer fluid.

We also work with two common 'hard-sphere'[20] colloidal systems: $2a = 1.54\ \mu$m plain silica spheres (Bang Laboratories, Inc.) and $2a = 1.45\ \mu$m sterically stabilized, fluorescent polymethylmethacrylate (PMMA) spheres (purchased from Andrew Schofield, the University of Edinburgh). These colloidal spheres are similar in size to the superballs, allowing for direct comparisons between the behavior of the colloidal spheres and superballs. The silica spheres were index matched using a similar glycerol/water mixture, adjusting the glycerol content to match the slightly lower refractive index (70 % glycerol mass fraction, refractive index $n = 1.426$, viscosity $\mu = 0.02$ Pa·s at 21.0 °C). The PMMA spheres were index matched using a cyclohexylmethyl bromide (CXB)/decalin mixture (73 % CXB mass fraction), with a small amount of tetrabutylammonium bromide salt to screen electrostatic interactions.

Confocal Imaging

To characterize the particle diffusion and suspension microstructure, we imaged and tracked particles in three dimensions using a Leica SP-5 laser scanning confocal microscope. Samples were prepared in plasma-cleaned glass capillaries sealed with UV epoxy and stored when not in use on a slowly rotating mixing wheel to prevent sedimentation. We restricted the imaging volume to at least 25 μm above the bottom surface and at least 100 μm from the sides of the capillary to avoid wall effects. The fluorescent PMMA spheres could be imaged readily and tracked using standard techniques.[21,22]

Locating the hollow superballs posed a challenge, since instead of a bright peak at the particle center, the fluorescent shells define the particle edges. In two-dimensional slices from a 3D image stack, the superball shaped shells can be picked up by a circular Hough transform to locate the (x,y) position of each particle. These positions were linked together

using tracking routines and averaged to locate the z position of each particle. To prevent multiple particles from being misidentified as a single object, we used an iterative routine to break apart tracks longer than 1.5 times the edge length of a superball. This routine can accurately locate the superball positions but requires high-contrast, high-resolution images, making high-speed three dimensional tracking challenging in moderately dense suspensions. While the the superball pair distribution function was measured using samples consisting solely of fluorescent superballs, diffusion measurements were carried out using undyed superballs with a small amount of fluorescent tracers. This allowed us to image larger volumes at reduced resolution and track tracer particles over long times (up to 3 h). In these measurements we fluroescently dyed the glycerol/water suspending fluid, allowing us to obtain negative images of the undyed superballs to measure the volume fraction for each sample.

Measuring Volume Fraction

To ensure that the composition and viscosity of the suspending fluid remained constant from sample to sample, suspensions with varying volume fraction $\phi = V_{part,tot}/V_{tot}$ were prepared by diluting moderately concentrated stock solutions, using the supernatant from the the final centrifugation step for the subsequent dilutions. We measure ϕ using confocal imaging to locate particles within a 3D volume and computing the Voronoi tessellation[23] from the measured particle positions. The total volume V_{tot} is the sum of all the cell volumes, excluding those on the boundaries, and $V_{part,tot} = n_{cells} v_{sb}(a,m)$, where n_{cells} is the number of cells and $v_{sb}(a,m)$ is the volume of a superball with size a and shape parameter m. The volume of a superball can be expressed analytically in terms of the Euler beta function $B(p,q) = \Gamma(p)\Gamma(q)/\Gamma(p+q)$ by[24]

$$v_{sb}(a,m) = \frac{8}{m^2} B\left(\frac{1}{m}, \frac{m+1}{m}\right) B\left(\frac{1}{m}, \frac{m+2}{m}\right) a^3, \quad (2)$$

which gives $v_{sb} \approx 5.53a^3$ for $m = 2.85$, roughly 32 % larger than a sphere of radius a.

Samples for diffusion measurements were all prepared from a single stock solution, while a separate stock was used for the superball rheology measurements. We directly measured the volume fraction of all samples used in the diffusion measurements. For the rheology we imaged a subset of the samples to determine ϕ for the stock solution and subsequent dilutions. Spatial variations in the measured volume fraction, uncertainty in the particle size and particle locating errors in the confocal images limit our relative uncertainty in ϕ to about 5 % to 7 %, e.g. $\phi = 0.37 \pm 0.02$. We used a similar procedure to measure the volume fraction in the hard sphere samples. The volume fraction in a sample can be roughly estimated by centrifuging a fixed volume and measuring the volume of the densely packed sediment and assuming random close packing in the sediment, using $\phi_{rcp} = 0.71$ for the superballs[25] and $\phi_{rcp} = 0.64$ for spheres. However we found this method tended to underestimate the volume fraction by roughly 10 % indicating that $\phi_{sed} < \phi_{rcp}$, a discrepancy which has also been observed by others.[19]

Rheology

The rheology of silica superballs and solid silica spheres was characterized under steady shear at 21.0 °C using an Anton-Paar MCR302 with a 25 mm cone-plate tool. A temperature control hood was used to minimize exposure to ambient moisture to prevent the hydroscopic glycerol-water index matching fluid from absorbing extra water. The sample was sheared at $\dot{\gamma} = 100$ s^{-1} for 10 min prior to collecting data to ensure the sample was uniformly mixed. For each sample we performed four back to back sweeps of the shear rate and observed minimal drift or hysteresis in the measured viscosity $\eta(\dot{\gamma})$. We varied the shear rate from $\dot{\gamma} = 10^0$ s^{-1} to $\dot{\gamma} = 10^3$ s^{-1}, covering a range of Péclet number $Pe = 6\pi\mu a^3\dot{\gamma}/k_BT$ from $Pe = 5.8 \times 10^2$ up to $Pe = 5.8 \times 10^5$. However the maximum Reynolds number for individual particles remains below $Re_p \leq 4^{-3}$ even at our maximum shear rate, so inertial effects remain negligible.

For dilute suspensions of silica spheres ($\phi < 0.15$) we also employed a double-gap Couette cell, though the sample volume requirements prevented us from using this cell with our superballs. While there were no significant differences between results obtained using the cone-plate tool and Couette cell, there is less scatter in measurements using the Couette cell. This is due to the large sample volume required for the Couette cell relative to the cone-plate tool (3.8 mL vs 75 μL), making the results much less sensitive to small pipetting errors or changes in the water content in the suspending fluid from absorbed ambient moisture.

3 Results and Discussion

Rheology and diffusion in dilute suspensions

In Fig. 2*A* we plot the relative viscosity $\eta(\dot{\gamma})/\mu$ of our superball suspensions at low to moderate volume fractions. Below $\phi \approx 0.25$ we observe Newtonian behavior, where the suspension viscosity is independent of shear rate and only depends on ϕ. This Newtonian viscosity $\eta_N(\phi)$ corresponds to the 'high-shear' limiting viscosity (sometimes denoted η_∞), since $Pe \gg 1$ even at our lowest shear rates.

In dilute suspensions ($\phi \lesssim 0.2$), the relative viscosity can be expanded as $\eta_N/\mu = 1 + [\eta]\phi + c_2\phi^2 + \mathcal{O}(\phi^3)$, where $[\eta]$ is the intrinsic viscosity. The intrinsic viscosity characterizes the hydrodynamic stresses acting on an isolated particle in a

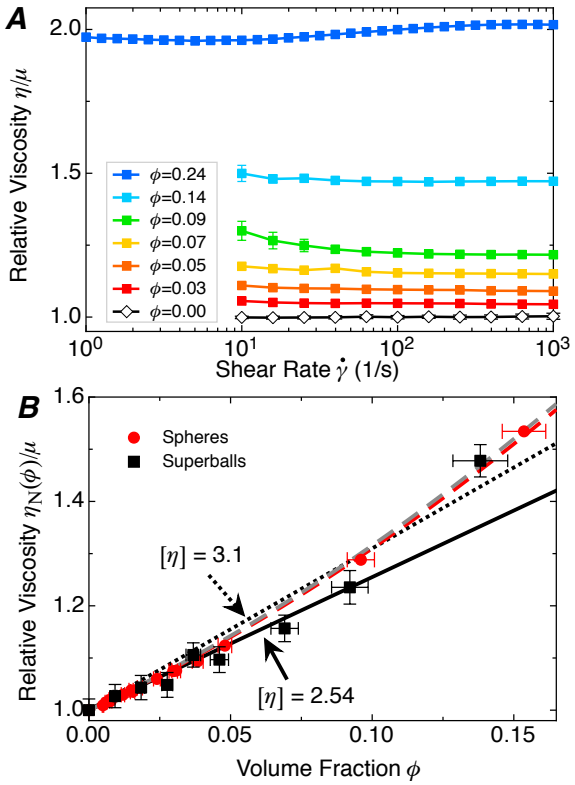

Fig. 2 Viscosity of dilute superball suspensions. (A) Relative viscosity η/μ versus shear rate $\dot{\gamma}$ for superball suspensions at various volume fractions. (B) Newtonian high-shear viscosity η_N/μ for superballs (black squares) and silica spheres (red circles) versus ϕ. Black lines show $\eta_N/\mu = 1+[\eta]\phi$ for $[\eta] = 2.54$ (solid line) and $[\eta] = 3.1$ (dotted line). Dashed lines include second order corrections: $\eta_N/\mu = 1+[\eta]\phi + c_2\phi^2$. Red dashed line: predicted hard-sphere values[26] $[\eta]^{HS} = 2.5$ and $c_2^{HS} = 6.0$. Grey dashed line: a fit to the superball results yields $c_2 = 6.2 \pm 0.4$. Error bars in (A) reflect variations in η over the course of repeated up and down shear sweeps, while in (B) they include uncertainty in $\mu = 0.292$ Pa·s $\pm$ 0.001 Pa·s.

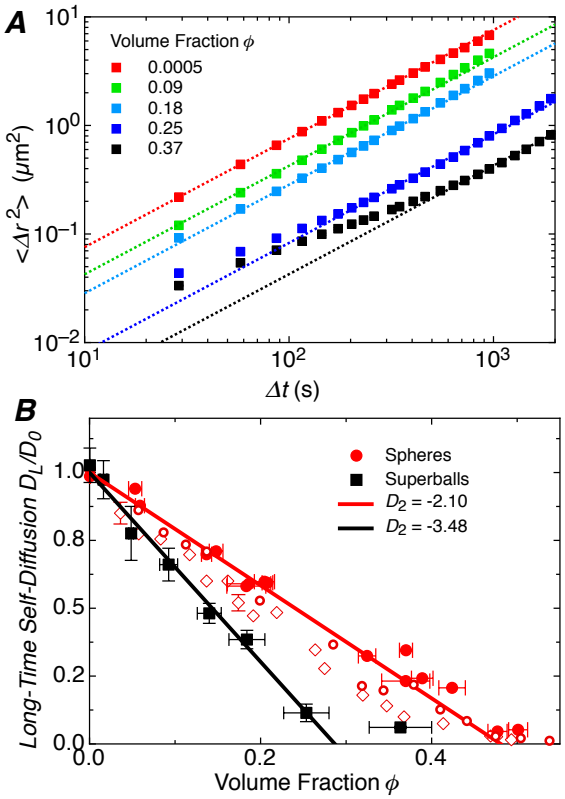

Fig. 3 Superball diffusion. (A) Mean squared displacement (MSD) of fluorescent tracer superballs tracked using 3D confocal microscopy. Dotted lines: fits to $\langle \Delta r^2 \rangle = 6D_L\Delta t$. (B) Long-time self diffusion coefficient $D_L(\phi)$ for superballs (black squares) and PMMA spheres (solid red circles). Error bars in (B) reflect the standard deviation from multiple measurements with the same sample. Solid lines: fits to $D_L(\phi) = D_0(1+D_2\phi)$ for $\phi \leq 0.20$. Red open symbols show data for D_L/D_0 for hard spheres from van Megen et al. obtained using tracer particles in a DLS setup. Open circles: $2a = 166$ nm poly(vinyl alcohol) spheres with $2a = 170$ nm PMMA tracers in decalin.[27] Open diamonds: $2a = 432$ nm PMMA spheres with $2a = 410$ nm silica tracers in a decalin/CS_2 mixture.[28]

simple shear flow,[29] and thus depends directly on the particle shape. For hard spheres $[\eta]^{HS} = 2.5$ and can be obtained analytically,[29,30] while a variety of numerical techniques are available to compute $[\eta]$ for more complex shapes.[10,31] Recent experimental work with PbTe and Fe_3O_4 nano-cubes found $[\eta] = 3.1$, in agreement numerical predictions.[12] This larger value is due to large hydrodynamic stresses near cube corners, which are blunted with our rounded cubic superballs. Recent numerical work[32] on the hydrodynamic properties of superballs over a range m found that for $m = 2.85$ the intrinsic viscosity is $[\eta] = 2.54$, only marginally above the hard sphere value.

A direct comparison between dilute suspensions of spheres and superballs (Fig. 2*B*) reveals little difference in the relative viscosity of the two types of particles. Fitting the superball viscosity for $\phi < 0.05$ to $\eta_N(\phi)/\mu = 1+[\eta]\phi$ yields $[\eta] = 2.57 \pm 0.11$, consistent with $[\eta] = 2.54$ predicted in ref. [32] and below $[\eta] = 3.1$ predicted for ideal cubes. The results for the silica spheres agree exceptionally well with both the the linear $[\eta]^{HS} = 2.5$ and second order $c_2^{HS} = 6.0$ coefficients predicted for ideal hard spheres (Fig. 2*B*). Including the second order term in the superball viscosity for $\phi < 0.15$ yields $c_2 = 6.2 \pm 0.4$, again giving a coefficient that is slightly higher than the comparable hard sphere value.

In Fig. 3*A* we plot the three dimensional mean squared displacement (MSD) $\langle \Delta r^2(\Delta t) \rangle = \langle [\vec{r}(t+\Delta t) - \vec{r}(t)]^2 \rangle$ for fluorescent tracer superballs over a range of ϕ. In dilute suspensions,

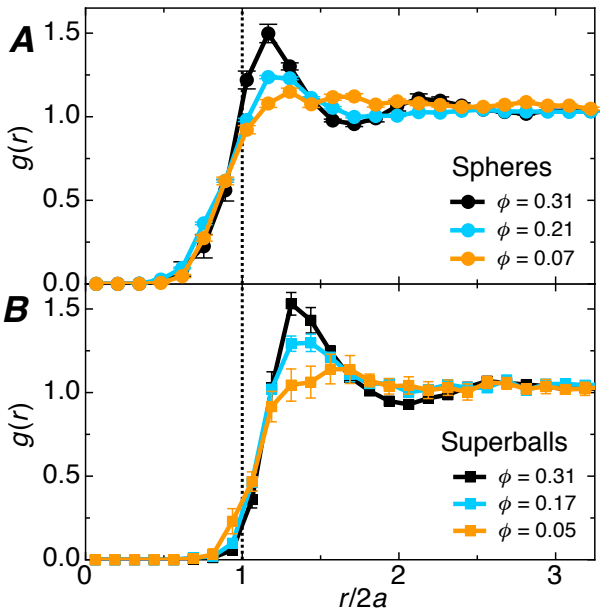

Fig. 4 Microstructure of superball and hard sphere suspensions. Pair distribution function $g(r)$ for suspensions of (A) superballs and (B) PMMA spheres at various volume fractions ϕ. The separation distance r is scaled by the average diameter $2a = 1.45$ μm for the PMMA spheres and by the average edge length $2a = 1.50$ μm for the superballs. Error bars reflect the standard deviation reflect the standard deviation from multiple measurements with the same sample.

diffusion slows down as ϕ increases but the MSD remains linear, allowing us to extract the long-time self-diffusion coefficient $D_L(\phi)$ by fitting $\langle \Delta r^2(\Delta t) \rangle = 6 D_L \Delta t$. At volume fractions above $\phi \approx 0.25$ the MSD is initially sub-diffusive before transitioning to diffusive motion at later times, when the root mean squared displacement is roughly a distance a. In these samples we restrict out fit to the late-time regime, where the MSD is linear, when computing $D_L(\phi)$.

We fit $D_L(\phi) = D_0(1 + D_2\phi)$ for $\phi \leq 0.2$ to extract the single particle diffusion constant D_0 and the first-order correction D_2. We obtain $D_0 = 1.14 \times 10^{-3}$ μm^2/s $\pm 0.06 \times 10^{-3}$ μm^2/s, giving an effective hydrodynamic diameter $d_H \equiv k_B T / 3\pi\mu D_0 = 1.59$ μm $\pm$ 0.11 μm. Most of the uncertainty in d_H is due to uncertainty in the viscosity of the glycerol/water supernatant μ. Our measured d_H is just slightly larger than the edge length ($d_H/2a = 1.06 \pm 0.08$) and consistent with recent numerical work by Audus *et al.*[32] which predicts $d_H/2a \approx 1.10$ for $m = 2.85$.

Diffusion and structure

When looking at single particle hydrodynamic properties such as the intrinsic viscosity $[\eta]$ and hydrodynamic diameter d_H, these superballs seem almost indistinguishable from hard-spheres. However, there is a clear difference between the superballs and hard spheres in how the diffusion slows down with increasing ϕ (Fig. 3*B*). Our measured $D_L(\phi)/D_0$ in the PMMA spheres is slightly above, but generally in agreement with previous experimental results[27,28] and the initial slope $D_2 = -2.08 \pm 0.01$ agrees well with the predicted value for hard spheres[29,33] $D_2^{HS} = -2.1$. However, in the superball suspensions we observe a significantly faster initial decrease in $D_L(\phi)/D_0$, with $D_2 = -3.48 \pm 0.19$. This difference in the long-time self diffusivity is evident even at relatively low volume fractions ($\phi < 0.20$), where we observe minimal differences in the relative viscosity of superball and hard sphere suspensions. This suggests that the difference in the long-time self diffusivity of the spheres and superballs is due to differences in the suspension microstructure.

We therefore compare the pair distribution function $g(r)$ for spheres and superballs at different volume fractions in Fig. 4. For PMMA spheres the measured pair distributions match expectations for a hard-sphere colloidal liquid (Fig. 4*A*). Theoretically, in mono-disperse hard spheres with radius a, the pair distribution $g(r) = 0$ for $r < 2a$ then jumps to a finite value g_m at contact $r = 2a$. In practice polydispersity and particle locating errors blur this jump, though the peak location is still close to $r = 2a$. At higher volume fractions the peak g_m increases, reflecting a growing number of particles in close contact, and damped oscillations appear for $r > 2a$, reflecting spatial correlations in the local density.[34] In superball suspensions, we observe similar trends in both the rise in the first peak and the development of oscillations as ϕ is increased.

With superballs there is no longer a single distance at which particles come into contact, but instead the conditions for contact depend on the relative particle orientations. The minimum possible separation between superballs with size a defined by Eq. 1 is $r = 2a$, corresponding to face-to-face contact. However, when scaling r by this minimum separation we find $g(r)$ for the superball suspensions is shifted to larger distances compared to the hard sphere $g(r)$, with the first peak occurring at a substantially larger separation (Fig. 5*A*). In Fig. 5*B* we show the same data, but replace a with an effective radius $a_{eff} = 3^{1/2-1/m} a$ defined by the minimal sphere needed to enclose a superball, i.e. the radius to the corner. This effective radius reduces to $a_{eff} = a$ for $m = 2$ (spheres), $a_{eff} = 3^{1/2} a$ for $m \to \infty$ (cubes) and for our superballs with $m = 2.85$ we have $a_{eff} \approx 1.18a$. Scaling by this effective radius matches both the location of the first peak and the oscillation period for the sphere and superball suspensions, so that the shifted pair distributions for the different particles at the same ϕ look nearly identical (Fig. 5*B*).

Motivated by this rescaling, in Fig. 5*C* we re-plot D_L/D_0 for the spheres and superballs against an effective volume fraction ϕ_{eff} defined by this minimal enclosing sphere. The effec-

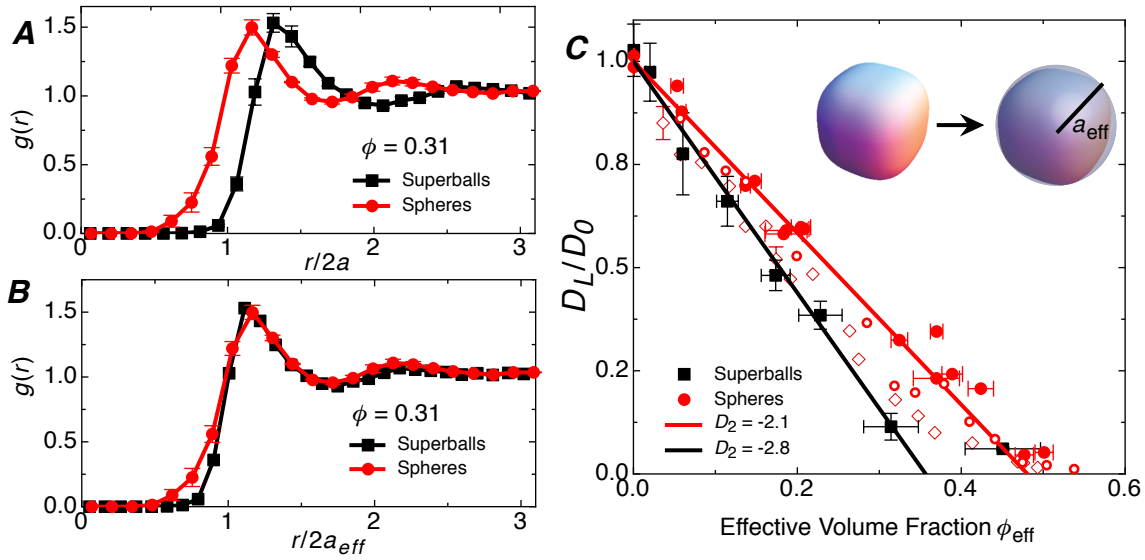

Fig. 5 Effective superball radius. (A) $g(r)$ for superballs (black squares) and PMMA spheres (red circles) at $\phi = 0.31$. Data and error bars are the same as in Fig. 4. (B) Same data with the separation distance r scaled by the effective diameter $2a_{eff}$, where $a_{eff} = 3^{1/2-1/m}a$ so that $a_{eff} = 1.18a$ for the superballs and $a_{eff} = a$ for the spheres. (C) D_L/D_0 for spheres and superballs (same data, symbols and error bars as in Fig. 3), with the superball data now plotted against the effective volume fraction ϕ_{eff} defined by the minimal enclosing sphere.

tive volume fraction is related to the physical volume fraction ϕ by

$$\phi_{eff} = \frac{\frac{4}{3}\pi a_{eff}^3}{v_{sb}(a,m)}\phi \qquad (3)$$

where $v_{sb}(a,m)$ is the volume of a superball given by Eq.2. For our particles with $m = 2.85$ the effective volume fraction is $\phi_{eff} \approx 1.24\phi$.

The first order corrections to $D_L(\phi)/D_0$ are proportional to terms of the form[33,35] $n\int_{2a}^{\infty} h(r)g(r)r^2dr$, where n is the particle number density, $h(r)$ characterizes different types of particle-particle interactions (hydrodynamic, etc) and the lower limit of integration reflects the fact that $g(r < 2a) = 0$ for hard spheres. For hard spheres we non-dimensionalize the integral by scaling $\tilde{r} = r/a$ to obtain a term proportional to $a^3 n \propto \phi$. We have shown that the sphere and superball pair distributions align when we replace $2a \to 2a_{eff}$, and if we assume the interaction terms contained in $h(\tilde{r})$ are similar for the spheres and superballs, then this first order correction for the superball long-time self diffusivity is the same as in the hard sphere case but with $a^3 n$ replaced with $a_{eff}^3 n \propto \phi_{eff}$. Rescaling by this effective volume fraction brings the superball and sphere long-time self diffusion results into closer agreement, though $D_L(\phi_{eff})/D_0$ for the superballs still falls slightly bellow the hard sphere data and a linear fit gives an initial slope $D_2 = -2.80 \pm 0.16$. This suggests that non-negligible differences in the hydrodynamic interactions $h(\tilde{r})$ remain.

This shape mediated excluded volume interaction might manifest itself in other quantities that depend on the particle interactions, such as the osmotic pressure. Collision-driven molecular dynamics (MD) simulations of dense superball suspensions by Batten et al.[24] show a similar shift in $g(r)$, however osmotic viral coefficients computed in that same study do not show this large excluded volume effect, for example $B_2/v_{sb} \approx 4.1$ for $m = 2.85$ while $B_2/v_{sph} = 4$ for hard spheres. It is possible that this difference is due to the additional hydrodynamic contributions contained in $h(r)$, or that the rotational diffusion needs to be better modeled to capture this effect.

The rotational diffusion coefficient $D_R(\phi)$ of hard spheres exhibits a much weaker dependence on ϕ than the translational diffusion coefficient.[36] Since the superball shape does not dramatically effect the single particle hydrodynamics, we expect the single particle rotational diffusion coefficient to be well approximated by the hard sphere value $D_{R,0} = 3D_0/4a^2$. The angular mean squared displacement is given by $\langle \Delta\theta^2 \rangle = 4D_R\Delta t$, so the timescale τ_R for a superball to diffuse a root mean squared angular distance $\Delta\theta = 0.96$ radians (from a corner to the center of a face) is $\tau_R \approx 150$ s. This timescale is somewhat shorter than the timescale for caged diffusion at higher volume fractions (Fig. 3*A*), and the MD simulations[24] of superballs found no rotational correlations in the fluid phase except for rare configurations with particles in perfect face-to-face contact. Together, this suggests that the superballs can explore the full range of orientations within their transient cages, so that their excluded volume is essentially set by the enclosing sphere radius a_{eff}.

In hard sphere suspensions, sub-diffusion and caged motion

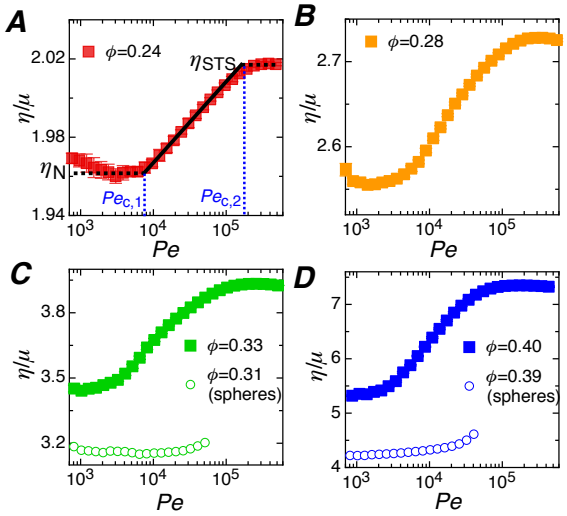

Fig. 6 Shear-thickening. (A)-(D) Relative viscosity η/μ versus Péclet number Pe for superballs (solid squares) and silica spheres (open circles in (C) and (D)) at various volume fractions. In (A) we illustrate how we define the Péclet number for the onset of shear thickening $Pe_{c,1}$ and the viscosity plateau $Pe_{c,2}$. Horizontal dashed lines show η_N/μ and η_{STS}/μ. The solid line is a fit to $\eta/\mu = A\ln Pe + B$ in the shear thickening region. $Pe_{c,1}$ and $Pe_{c,2}$ are determined by the intercepts at η_N/μ and η_{STS}/μ, respectively.

becomes noticeable at volume fractions as low as $\phi = 0.32$ and typically becomes pronounced for $\phi > 0.4$.[37,38] We first observe sub-diffusion at $\phi = 0.25$ and at $\phi = 0.37$ the sub-diffusion is quite pronounced, indicating enhanced caging in the superball suspensions. In terms of the effective volume fraction ($\phi_{eff} = 0.30$ and $\phi_{eff} = 0.44$) the sub-diffusion observed in these two samples aligns much closer with the onset of sub-diffusion in hard spheres, suggesting the short-time caging dynamics are also controlled by this shape mediated interaction.

We cannot directly apply this rescaling $\phi \to \phi_{eff}$ to the suspension viscosity $\eta_N(\phi)/\mu$, since the viscosity contains contributions from both the single particle hydrodynamics and the suspension microstructure. When expanding η_N/μ in powers of ϕ, the linear term $[\eta]\phi$ remains unchanged since it is independent of $g(r)$. Higher order terms reflect the coupling between the hydrodynamics and structure, resulting in mixed terms that depend on both the physical volume fraction ϕ and the effective volume fraction ϕ_{eff}. For details see the SI and refs. [39] and [40], which address the relative hydrodynamic and interaction contributions to the viscosity of core-shell particles.

Shear thickening at moderate volume fractions

As the volume fraction in a sheared suspension is increased, the coupling between the suspension microstructure and hydrodynamic interactions becomes increasingly important and we expect likewise the details of the particle shape to become increasingly important. Indeed, we find that at moderate volume fractions as low as $\phi = 0.24$ the superball suspensions exhibit non-Newtonian shear thickening behavior (Fig. 6). The superball suspensions exhibit mild shear thinning at our lowest shear rates (or equivalently Péclet numbers Pe). The viscosity then plateaus at the high-shear Newtonian viscosity $\eta_N(\phi)$. At a Péclet number $Pe_{c,1}$ the viscosity begins to rise logarithmically over a decade in Pe. At a second value of the Péclet number $Pe_{c,2}$ the viscosity plateaus at a higher value η_{STS}. Over the range of volume fractions explored here the ratio η_{STS}/η_N varies between $\eta_{STS}/\eta_N = 1.04$ at $\phi = 0.24$ to $\eta_{STS}/\eta_N = 1.4$ at $\phi = 0.40$, a rather mild increase compared to the large viscosity increases that have been observed in discontinuous shear thickening suspensions.[41,42] The shear thickening observed in these superball suspensions is reversible, with no discernible hysteresis when repeatedly increasing and decreasing the shear rate.

While we begin to see hints of shear thickening in our silica sphere suspensions at similar volume fractions (Figs. 6*C-D*), the shear thickening in the superball suspensions begins at much lower Péclet numbers. The critical Péclet numbers for shear thickening onset $Pe_{c,1}$ and the viscosity plateau $Pe_{c,2}$ in the superball suspensions both decrease with increasing volume fraction. However, if we plot the viscosity against the physical shear stress $\sigma = \eta\dot{\gamma}$, we find that both the onset stress $\sigma_{c,1}$ and plateau stress $\sigma_{c,2}$ are roughly constant, independent of ϕ (Fig. 7). In the superballs, the average onset stress is $\langle\sigma_{c,1}\rangle = 4.7$ Pa ± 1.3 Pa, while the viscosity plateau occurs at a stress $\langle\sigma_{c,2}\rangle = 119.5$ Pa ± 15.7 Pa.

Comparing the form of $\eta(\sigma)/\eta_N$ for suspensions of superballs and silica spheres over a range of ϕ in Fig. 7, we find that the rescaling $\phi \to \phi_{eff}$ cannot account for the difference between the shear thickening in the two types of particles. In the silica sphere suspensions, the shear thickening onset occurs at a stress $\sigma_c \approx 20$ Pa, independent of the ϕ and well above the onset stress in the superball suspensions. We do not observe a comparable viscosity plateau in the sphere suspensions for $\phi < 0.5$ within our measured shear stresses. In sphere suspensions at higher volume fractions ($\phi \approx 0.6$), where the shear thickening becomes discontinuous, the viscosity begins to approach a plateau around 10^3 Pa, again much higher than the plateau stress for the superball suspensions.

While the microscopic origins of shear thickening remains a subject of active research and debate,[41,42] continuous shear thickening in colloidal suspensions is typically ascribed to large lubrication forces that develop as particles are driven into

close contact, creating particle clusters that are tightly coupled by these hydrodynamic forces.[43–45] In this scenario, many-body effects conspire to force particles into close contact, so the gaps between particle surfaces δ approaches 0, while hydrodynamic lubrication forces diverge as $1/\delta$. In real colloidal systems the 'hard-sphere' picture breaks down as $h \to 0$ and details of the surface interactions (i.e., a polymer brush or short-ranged electrostatics) become important. The minimum separation δ_m is set by balancing the shear stress and some repulsive contact force F_{rep}. Shear thickening occurs when the contact relaxation time[45] $\tau_{cont} = \alpha(\delta_m)/k(\delta_m)$ becomes longer than the shear timescale $1/\dot{\gamma}$. For hard spheres, $\alpha = 3\pi\eta a^2/2\delta$ is the lubrication drag coefficient and $k = dF_{rep}/d\delta$ an effective spring constant evaluated at δ_m. For short ranged electrostatic repulsion with a surface potential ψ_s, this stress is given by[46,47] $\sigma_c \approx 0.1(\pi\varepsilon_r\varepsilon_0\psi_s^2\kappa/a)$. For $\sigma_c \approx 20$ Pa exhibited by the silica spheres, this translates to $\psi_s = -31$ mV, a reasonable value for colloidal silica.[48]

At present there is no theory for the critical onset stress for shear thickening in suspensions of shaped particles. For such particles, both the lubrication and contact forces will depend on the relative particle orientations. While tangential forces play a negligible role in the traditional picture for lubrication-driven shear thickening,[45] in shaped particles the role of particle rotations should become increasingly important, particularly at higher volume fractions. Given the nearly identical particle compositions and suspending fluids, the surface potential for the spheres and superballs should be nearly the same. While it is possible that the difference between the onset stresses in the spheres and superballs can be accounted for by appropriately modifying the lubrication and electrostatic forces, it is also possible that different modes of stress transmission and relaxation need to be considered.

The second, high-stress viscosity plateau in the shear thickened state has been observed by others in suspensions of spherical particles, though the origin of this plateau remain unresolved.[49,50] We speculate that the viscosity plateau in the superball suspensions at $\sigma_{c,2}$ reflects a structural change that allows the superballs to relieve large lubrication stresses, though additional studies exploring the dynamics and structure at high shear rates and volume fractions is needed to examine this transition.

To characterize the increase in the superball viscosity at higher volume fractions, we fit both $\eta_N(\phi)$ and $\eta_{STS}(\phi)$ to a Kreiger-Dougherty type equation:

$$\frac{\eta}{\mu} = (1-\phi/\phi_m)^{-[\eta]\phi_m} \quad (4)$$

in Fig. 8. We employ this function as an empirical fit, fixing $[\eta] = 2.54$ to fit the data in the dilute limit and allowing ϕ_m to vary. This yields $\phi_m^{STS} = 0.56 \pm 0.04$ in the shear thickened state and $\phi_m^N = 0.68 \pm 0.07$ in the high-shear Newtonian

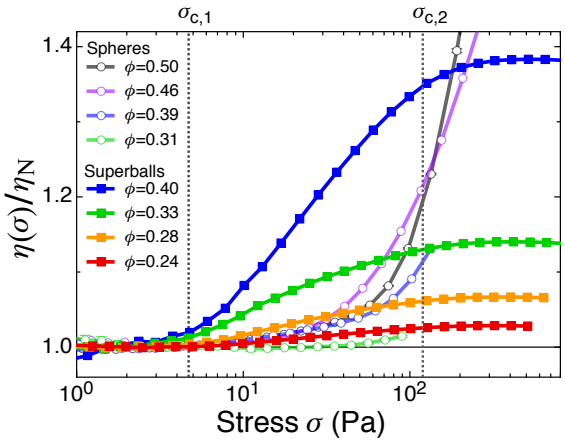

Fig. 7 Shear thickening onset. Viscosity (scaled by $\eta_N(\phi)$) plotted against shear stress $\sigma = \eta\dot{\gamma}$ for superballs (solid squares) and silica spheres (open circles). Vertical dotted lines show the average values $\langle\sigma_{c,1}\rangle = 4.7$ Pa ± 1.3 Pa and $\langle\sigma_{c,2}\rangle = 119.5$ Pa ± 15.7 Pa. The range of superball volume fractions $0.24 \le \phi \le 0.40$ corresponds to a range $0.30 \le \phi_{eff} \le 0.50$ using the same rescaling $\phi_{eff} = 1.24\phi$ using in Fig. 5.

regime at stresses below the shear thickening onset. We also plot this function with fixed $[\eta] = 2.5$ and $\phi_m^{HS} = 0.71$ which was previously found to fit the high-shear Newtonian viscosity in hard-sphere suspensions.[26,51,52] Our measured viscosities in the silica spheres agree quite well with this previous result for $\phi < 0.5$. The extracted ϕ_m^N for the superballs is slightly lower than ϕ_m^{HS} for hard spheres, though this difference is less than the uncertainty in ϕ_m^N. Recent work[50] examining η_{STS} in strongly shear thickening suspensions of silica spheres ($a = 260$ nm) suspended in poly-ethylene glycol ($M_w = 200$) found $\phi_m^{STS} = 0.54 \pm 0.01$, close to our measured ϕ_m^{STS}. One might expect the viscosity divergence in superballs to occur at a *higher* volume fraction, since the maximum volume fractions for disordered and crystalline packings of superballs exceed the maximum volume fractions possible in sphere packings.[24] Other functional forms have been proposed to describe the divergence of the high-shear viscosity in concentrated suspensions,[50,51] however alternative forms do not significantly change the quality of the fits or the extracted values of ϕ_m. More data at higher volume fractions is needed to better resolve the behavior of highly concentrated superball suspensions.

4 Conclusions

Our results highlight the challenges and subtleties inherent in adapting results and theories for uniform spheres to suspensions of anisotropic, shaped particles. Superballs seem simple at the single particle level, with hydrodynamic proper-

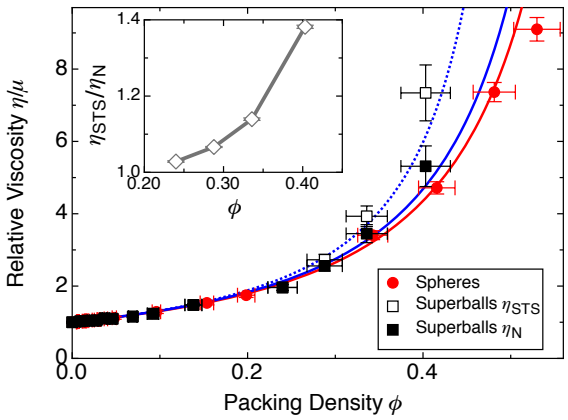

Fig. 8 Relative viscosity at higher concentrations. Relative viscosity for superballs in the high-shear Newtonian regime η_N (filled squares), in the shear thickened plateau η_{STS} (open squares). Also shown is η_N for silica spheres (red circles). Solid red line: Eq. 4 with fixed $[\eta] = 2.5$ and $\phi_m = 0.71$. Blue lines: fits to Eq. 4 with $[\eta] = 2.55$ held fixed and ϕ_m allowed to vary for η_N (solid blue line) and η_{STS} (dotted blue line). Fits yield $\phi_m^{STS} = 0.56 \pm 0.04$ and $\phi_m^N = 0.68 \pm 0.07$.

ties (characterized by the hydrodynamic diameter d_h and intrinsic viscosity $[\eta]$) that are marginally different from hard spheres. However, the particle shape modifies the suspension microstructure (characterized by $g(r)$), which significantly alters the diffusive behavior of the superballs (measured by $D_L(\phi)$). Similarly, the shear thickening at moderate concentrations is qualitatively different from the shear thickening we observe in comparable hard spheres.

The differences between the hydrodynamic contributions to the viscosity and the shape-mediated contributions to the self-diffusion highlight the challenges in applying Generalized Stokes Einstein (GSE) relations[53–55] to suspensions of shaped particles. These GSE relations relate the viscosity and diffusion $\eta(\phi)/\mu = C(\phi)D_0/D(\phi)$, where a constant $C(\phi) = 1$ would correspond to a strict GSE relation. While we expect the diffusion and viscosity to follow a similar trend, there is no fundamental reason this GSE relation must be strictly obeyed[54,55] and a variety of different forms of this GSE have been proposed, using either self-diffusion coefficient, collective diffusion coefficient[53,54] or Laplace transformed forms of frequency-dependent quantities.[56] Mode coupling theory[55] for hard spheres suggest a GSE relating the long-time self-diffusion and the zero-shear viscosity holds approximately with $C(\phi) \approx 1$ for $0 \leq \phi < 0.5$, though experimental evidence is mixed[19,54]. There must be finite deviations in dilute hard sphere suspensions, since one can expand $C(\phi) = 1 + ([\eta] + D_2)\phi + \ldots$ and $[\eta]^{HS} + D_2^{HS} = 0.4$. Though we measure the high-shear viscosity instead of the zero-shear viscosity in this work, the intrinsic viscosity should be the same in both limits. This indicates that deviations from $C(\phi) \approx 1$ in the superballs should be more pronounced and go in the opposite direction, since $[\eta] + D_2 = -0.93$. Relations of this form also fail in suspensions of charged spheres,[57] suggesting that the approximate agreement in hard spheres is coincidental, and GSE relations should not be expected to hold in suspensions where the single particle hydrodynamics and particle interactions are not simply related.

While it is possible to separate contributions from the single particle hydrodynamics and shape-mediated interactions in the viscosity and diffusion measurements in dilute suspensions, in moderately concentrated shear thickening suspensions the microstructure and hydrodynamic interactions are tightly coupled. In the hydrodynamic clustering picture of continuous shear thickening[41,43,58] with spherical particles, the dynamics is controlled by diverging pair-wise lubrication forces acting normal to the particle contacts, while tangential forces exhibit a slower logarithmic divergence with the gap size. In spheres, these forces furthermore depend only on the gap size and the only pathway to relax these forces is for Brownian or shear-induced diffusion to move particles apart from each other. This is no longer true with non-spherical particles.

Lubrication forces will depend strongly on the relative orientations of neighboring superballs, with the potential for both stronger lubrication forces at face-to-face contacts and weaker forces at edges or corners where the local radius of curvature is smaller. Furthermore, particle rotations provide a new route to relax lubrication stresses, particularly in corner or edge facing contacts. Previous studies have begun to explore the role particle shape plays in setting the range of volume fractions[14,15] where shear thickening is observed and how different shapes provide multiple avenues for stress to relax,[59] however more work is needed with well-controlled and characterized particle shapes.

Furthermore, in non-spherical particles translational and rotational motion are directly coupled, suggesting an analogy to contact friction in spherical particles. A growing body of evidence[42,49,60–62] suggests that discontinuous shear thickening, where the stress rapidly rises by orders of magnitude with increasing $\dot{\gamma}$, in non-Brownian suspensions is driven by dilation and frictional contact forces. Discontinuous shear thickening is also observed in (Brownian) colloidal suspensions, though the role of contact friction in this regime is less established. While we observe only mild shear thickening in the superballs over the range of volume fractions and shear stress explored here, we might expect more dramatic effects at higher volume fractions. More experimental work, as well as theory and simulations, are needed to better understand concentrated superball suspensions, and could potentially open a new window to address long debated questions in colloidal science.

Acknowledgements

We thank D. Audus and J. Douglas for insightful discussions and for sharing computational results. We also thank L. Rossi and S. Sacanna for advice on the superball synthesis. J.R.R. gratefully acknowledges the support of a NIST National Research Council postdoctoral fellowship. Certain instruments and materials are identified in this paper to adequately specify the experimental details. Such identification does not imply recommendation by the National Institute of Standards and Technology nor does it imply the materials are necessarily the best available for the purpose.

References

1 S. C. Glotzer and M. J. Solomon, *Nature Mater*, 2007, **6**, 557–562.
2 A. B. Pawar and I. Kretzschmar, *Macromol. Rapid Comm.*, 2010, **31**, 150–168.
3 S. Sacanna and D. J. Pine, *Curr. Opin. Colloid In.*, 2011, **16**, 96–105.
4 S. Torquato and Y. Jiao, *Nature*, 2009, **460**, 876–879.
5 P. F. Damasceno, M. Engel and S. C. Glotzer, *Science*, 2012, **337**, 453–457.
6 R. Ni, A. P. Gantapara, J. de Graaf, R. van Roij and M. Dijkstra, *Soft Matter*, 2012, **8**, 8826–8834.
7 D. Zerrouki, J. Baudry, D. Pine, P. Chaikin and J. Bibette, *Nature*, 2008, **455**, 380–382.
8 J. B. Hubbard and J. F. Douglas, *Phys. Rev. E*, 1993, **47**, R2983–R2986.
9 H. Zhou, A. Szabo, J. F. Douglas and J. B. Hubbard, *J. Chem. Phys.*, 1994, **100**, 3821–3826.
10 M. L. Mansfield, J. F. Douglas and E. J. Garboczi, *Phys. Rev. E*, 2001, **64**, 061401.
11 D. J. Kraft, R. Wittkowski, B. ten Hagen, K. V. Edmond, D. J. Pine and H. Löwen, *Phys. Rev. E*, 2013, **88**, 050301.
12 R. K. Mallavajula, D. L. Koch and L. A. Archer, *Phys. Rev. E*, 2013, **88**, 052302.
13 B. D. Leahy, X. Cheng, D. C. Ong, C. Liddell-Watson and I. Cohen, *Phys. Rev. Lett.*, 2013, **110**, 228301.
14 R. G. Egres and N. J. Wagner, *J. Rheol.*, 2005, **49**, 719–746.
15 E. Brown, H. Zhang, N. A. Forman, B. W. Maynor, D. E. Betts, J. M. DeSimone and H. M. Jaeger, *Phys. Rev. E*, 2011, **84**, 031408.
16 L. Rossi, S. Sacanna, W. T. M. Irvine, P. M. Chaikin, D. J. Pine and A. P. Philipse, *Soft Matter*, 2011, **7**, 4139–4142.
17 J.-M. Meijer, F. Hagemans, L. Rossi, D. V. Byelov, S. I. R. Castillo, A. Snigirev, I. Snigireva, A. P. Philipse and A. V. Petukhov, *Langmuir*, 2012, **28**, 7631–7638.
18 C. Graf, D. L. J. Vossen, A. Imhof and A. van Blaaderen, *Langmuir*, 2003, **19**, 6693–6700.
19 W. C. K. Poon, E. R. Weeks and C. P. Royall, *Soft Matter*, 2012, **8**, 21–30.
20 C. P. Royall, W. C. K. Poon and E. R. Weeks, *Soft Matter*, 2013, **9**, 17–27.
21 J. C. Crocker and D. G. Grier, *J. Colloid Interface Sci.*, 1996, **179**, 298.
22 E. R. Weeks and D. Weitz, *Chemical Physics*, 2002, **284**, 361 – 367.
23 C. H. Rycroft, *Chaos*, 2009, **19**, 041111–1.
24 R. D. Batten, F. H. Stillinger and S. Torquato, *Phys. Rev. E*, 2010, **81**, 061105.
25 Y. Jiao, F. H. Stillinger and S. Torquato, *Phys. Rev. E*, 2010, **81**, 041304.
26 W. B. Russel, N. J. Wagner and J. Mewis, *J. Rheol.*, 2013, **57**, 1555–1567.
27 W. van Megen, S. M. Underwood, R. H. Ottewill, N. S. J. Williams and P. N. Pusey, *Faraday Discuss. Chem. Soc.*, 1987, **83**, 47–57.
28 W. van Megen and S. M. Underwood, *J. Chem. Phys.*, 1989, **91**, 552–559.
29 W. Russel, D. Saville and W. Schowalter, *Colloidal Dispersions*, Cambridge University Press, 1992.
30 J. Mewis and N. Wagner, *Colloidal Suspension Rheology*, Cambridge University Press, 2011.
31 M. L. Mansfield and J. F. Douglas, *Phys. Rev. E*, 2008, **78**, 046712.
32 D. J. Audus, A. M. Hassan, E. J. Garboczi and J. F. Douglas, *Soft Matter*, 2015, **11**, 3360 – 3366.
33 B. Cichocki and B. U. Felderhof, *J. Chem. Phys.*, 1988, **89**, 3705–3709.
34 R. Kurita and E. R. Weeks, *Phys. Rev. E*, 2010, **82**, 011403.
35 B. Cichocki and B. U. Felderhof, *J. Chem. Phys.*, 1988, **89**, 1049–1054.
36 M. H. J. Hagen, D. Frenkel and C. P. Lowe, *Physica A*, 1999, **272**, 376–391.
37 A. Kasper, E. Bartsch and H. Sillescu, *Langmuir*, 1998, **14**, 5004–5010.
38 E. R. Weeks, J. C. Crocker, A. C. Levitt, A. Schofield and D. A. Weitz, *Science*, 2000, **287**, 627–631.
39 J. Bergenholtz, J. F. Brady and M. Vicic, *J. Fluid Mech.*, 2002, **456**, 239–275.
40 B. Cichocki, M. L. Ekiel-Jeżewska and E. Wajnryb, *Colloid Surface A*, 2013, **418**, 22–28.
41 N. J. Wagner and J. F. Brady, *Physics Today*, 2009, **62**, 27–32.
42 E. Brown and H. M. Jaeger, *Rep. Prog. Phys.*, 2014, **77**, 046602.
43 D. R. Foss and J. F. Brady, *J. Fluid Mech.*, 2000, **407**, 167–200.
44 B. J. Maranzano and N. J. Wagner, *J. Chem. Phys.*, 2001, **114**, 10514–10527.
45 J. R. Melrose and R. C. Ball, *J. Rheol.*, 2004, **48**, 937–960.
46 B. J. Maranzano and N. J. Wagner, *J. Rheol.*, 2001, **45**, 1205–1222.
47 Y. Lee and N. Wagner, *Rheologica Acta*, 2003, **42**, 199–208.
48 W. A. Ducker, T. J. Senden and R. M. Pashley, *Langmuir*, 1992, **8**, 1831–1836.
49 E. Brown and H. M. Jaeger, *J. Rheol.*, 2012, **56**, 875–923.
50 C. D. Cwalina and N. J. Wagner, *J. Rheol.*, 2014, **58**, 949–967.
51 C. G. de Kruif, E. M. F. van Iersel, A. Vrij and W. B. Russel, *J. Chem. Phys.*, 1985, **83**, 4717–4725.
52 J. C. van der Werff and C. G. de Kruif, *J. Rheol.*, 1989, **33**, 421–454.
53 A. L. Kholodenko and J. F. Douglas, *Phys. Rev. E*, 1995, **51**, 1081–1090.
54 P. N. Segrè, S. P. Meeker, P. N. Pusey and W. C. K. Poon, *Phys. Rev. Lett.*, 1995, **75**, 958–961.
55 A. J. Banchio, J. Bergenholtz and G. Nägele, *Phys. Rev. Lett.*, 1999, **82**, 1792–1795.
56 T. G. Mason and D. A. Weitz, *Phys. Rev. Lett.*, 1995, **74**, 1250–1253.
57 A. Imhof, A. van Blaaderen, G. Maret, J. Mellema and J. K. G. Dhont, *J. Chem. Phys.*, 1994, **100**, 2170–2181.
58 J. F. Brady and G. Bossis, *J. Fluid Mech.*, 1985, **155**, 105–129.
59 R. C. Kramb and C. F. Zukoski, *J. Rheol.*, 2011, **55**, 1069–1084.
60 R. Seto, R. Mari, J. F. Morris and M. M. Denn, *Phys. Rev. Lett.*, 2013, **111**, 218301.
61 R. Mari, R. Seto, J. F. Morris and M. M. Denn, *J. Rheol.*, 2014, **58**, 1693–1724.
62 M. Wyart and E. Cates, M. *Phys. Rev. Lett.*, 2014, **112**, 098302.